



REVIEW ARTICLE

Catalytic reduction of NO_x and oxidation of dichloroethane over α-MnO₂ catalysts: Properties-Reactivity relationship



Xin Ling ^{a,1}, Zhenghui Chen ^{a,1}, Bo Zhao ^e, Hua Pan ^{b,*}, Jun Chen ^{a,b}, Zeyu Wang ^b, Xuming Zhang ^{c,d}, Zhiping Ye ^{a,*}

^a Engineering Research Center of the Ministry of Education for Bioconversion and Biopurification, Zhejiang University of Technology, Hangzhou 310032, China

^b Laboratory of Pollution Exposure and Health Intervention Technology, College of Biological and Environment Engineering, Zhejiang Shuren University, Hangzhou 310015, China

^c School of Mechanical Engineering and Automation, Zhejiang Sci-Tech University, Hangzhou 310018, China

^d Huai'an Inyeng Environmental Technology Co., Ltd, Huai'an 223400, China

^e Zhejiang TUNA Environmental Science & Technology Co., Ltd., Shao'xing 312000, China

Received 6 July 2022; accepted 11 January 2023

Available online 18 January 2023

KEYWORDS

α-MnO₂;
NO_x reduction;
DCE oxidation;
Properties-reactivity
relationship

Abstract The reduction ability of NO to N₂ and the oxidation performance of 1,2-dichloroethane (DCE) over α-MnO₂ catalysts were investigated. The results show that α-MnO₂-3 exhibited the highest catalytic activity in 63.5 % conversion of NO_x reduction by C₃H₈ at 250 °C, and 80 % conversion of DCE combustion by O₂ at 338 °C. It is revealed the active phase of α-MnO₂-3 is tetragonal α-MnO₂ with the selectively exposed plane of (211). It was proposed the high DCE decomposition of α-MnO₂-3 was ascribed to the redox properties. The overall characterization results revealed that α-MnO₂-3 catalyst preserves more active sites of low valence Mn and higher surface adsorbed oxygen (O_{ads}) /lattice oxygen (O_{latt}) at the outermost layers, and lower reduction temperature in H₂-TPR profiles than that of other catalysts. Meanwhile, NH₃-TPD profile of α-MnO₂-3 also shows a large number of acid sites promote NO_x reduction.

© 2023 The Author(s). Published by Elsevier B.V. on behalf of King Saud University. This is an open access article under the CC BY-NC-ND license (<http://creativecommons.org/licenses/by-nc-nd/4.0/>).

* Corresponding authors.

E-mail addresses: panhua@zjsru.edu.cn (H. Pan), zhipingye@zjut.edu.cn (Z. Ye).

¹ These authors contributed equally to this work.

Peer review under responsibility of King Saud University.



1. Introduction

Waste incineration is developing rapidly in China, since this process can reduce waste volume as well as generate heat energy (Zhu et al., 2018). However, it cannot be avoidable to have pollutants, such as NO_x and chlorine-containing volatile organic compounds (CVOCs) from flue gas of municipal solid waste incinerators, and the emissions are increasing in recent years in China (Kulkarni et al., 2008; Wu et al., 2016; Li et al., 2017; Shao et al., 2021). Meanwhile, NO_x and CVOCs are the critical precursors of $\text{PM}_{2.5}$ and O_3 (Ni et al., 2009; Wu et al., 2016; Ye et al., 2022), which can cause severe environmental problems (Alzaky and Li, 2021). Therefore, how to effectively control emissions of NO_x and CVOCs has been a focus of air pollution control.

Selective catalytic reduction of NO_x by hydrocarbons (HC-SCR) has attracted much attention over the past two decades (More et al., 2018; Xu et al., 2020). The transition metal oxides display the good reactivity with inexpensive costs, which are becoming potential catalysts in HC-SCR, especially Mn-based catalysts. For example, Liu et al. (Liu et al., 2019a) obtained up to 100 % NO conversion at 130°C with MnO_x/AC in C_2H_4 -SCR.

In the last few decades, it has been emerging various strategies for VOCs elimination, such as adsorption (Zhao et al., 2022), plasma (Yu et al., 2020), biodegradation (Khan et al., 2018), catalysis (Chen et al., 2022), photocatalysis (Chen et al., 2022), Photothermal Catalysis (Yang et al., 2022b). Catalytic oxidation is recognized as one of the most efficient technologies for low concentration CVOCs removal due to high removal efficiency and mineralization rate (Fang et al., 2019; He et al., 2019; Liu et al., 2019c). Interestingly, transition metal oxides-based (MnO_x) catalysts with variable valance states also exhibit the potential of high reactivity in CVOCs decomposition (Kim and Shim, 2010; Santos et al., 2010; Piumetti et al., 2015; Ye et al., 2021). Sphere-Shaped Mn_3O_4 exhibited a complete conversion of methyl – ethyl – ketone to CO_2 at 200 °C (Pan et al., 2017). Cheng et al. (Cheng et al., 2017) also obtained 90 % dimethyl ether conversion at 238 °C on $\alpha\text{-MnO}_2$.

Hence, MnO_x catalysts shows the bifunctional ability to reduce NO_x and oxidize CVOCs. However, to the best of our knowledge, the promising catalyst of $\alpha\text{-MnO}_2$ in these two different reaction mechanisms was seldom reported when applying for NO_x reduction in HC-SCR and CVOCs oxidation separately. It is worthy investigating the relationship between structure properties and reactivity of $\alpha\text{-MnO}_2$, and to discuss the physicochemical characterizations. In this present work, a series of $\alpha\text{-MnO}_2$ catalysts with the different physical–chemical characteristics were prepared and applied for the catalytic removal of both NO_x and DCE (as the typical pollutant of CVOCs). Catalyst characterization and reactivity were investigated to illustrate the relation between properties and reactivity of $\alpha\text{-MnO}_2$ catalysts.

2. Materials and methods

2.1. Catalyst preparation

All $\alpha\text{-MnO}_2$ samples were synthesized by hydrothermal method using Potassium permanganate (KMnO_4) and Manganous acetate ($(\text{CH}_3\text{COO})_2\text{Mn}$) as precursors. For $\alpha\text{-MnO}_2\text{-1}$, 1.5 g $(\text{CH}_3\text{COO})_2\text{Mn}$ and 2.5 g KMnO_4 were added into 160 mL distilled water with magnetic stirring for 30 min at room temperature. Next, the mixed solution was poured into two Teflon-lined stainless-steel autoclave (100 mL), and then heated at 160 °C for 12 h. The obtained colloids were washed with deionized water and ethanol, then dried in vacuum at 80 °C for 12 h. The dried samples were calcined at 450 °C for 4 h. Finally, the catalyst was pelleted, crushed, and sieved to 40 ~ 60 mesh granules before use.

To modify the physical–chemical characteristics of $\alpha\text{-MnO}_2$ catalysts, the mass ratio of $(\text{CH}_3\text{COO})_2\text{Mn}$ and KMnO_4 was 4.9:3.2, and the temperature of hydrothermal treatment was 140 °C. The obtained product was donated as $\alpha\text{-MnO}_2\text{-2}$. Also, according to the synthesis plan of $\alpha\text{-MnO}_2\text{-1}$, the mass ratio of $(\text{CH}_3\text{COO})_2\text{Mn}$ and KMnO_4 was 9.7:6.3, and the temperature of hydrothermal treatment was 90 °C. The obtained product was donated as $\alpha\text{-MnO}_2\text{-3}$. To obtain $\alpha\text{-MnO}_2\text{-4}$, the mass ratio of $(\text{CH}_3\text{COO})_2\text{Mn}$ and KMnO_4 was 0.8:3.0, and the hydrothermal treatment was carried out at 240 °C.

2.2. Catalytic activity test

2.2.1. HC-SCR

The catalytic activity test of HC-SCR was carried out in a stainless-steel tubular (i.d.10 mm). 600 mg catalyst was evaluated under a typical feed gas included 800 ppm NO , 600 ppm C_3H_8 , 6.5 vol% O_2 , and N_2 as balance. The reaction temperature was conducted from 150 to 550 °C at a total flow rate of 450 mL/min, corresponding to a weigh hourly space velocity of 19 000 $\text{mL}\cdot\text{g}^{-1}\cdot\text{h}^{-1}$. The NO_x concentration of the inlet and

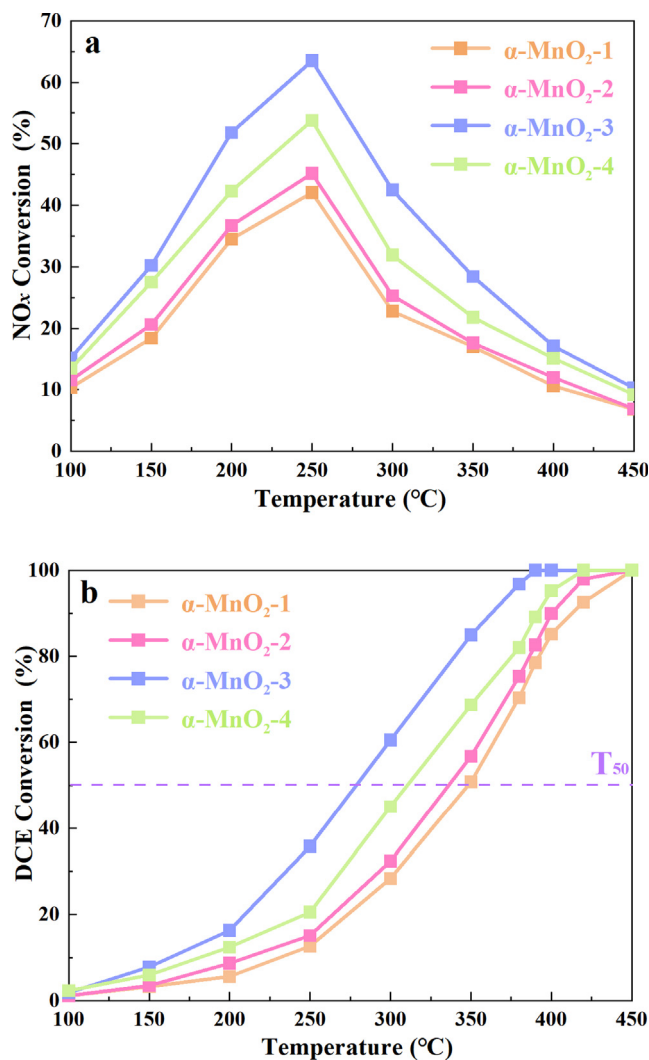


Fig. 1 NO_x (a) and DCE (b) conversion efficiencies as a function of temperature over a series of $\alpha\text{-MnO}_2$ samples.

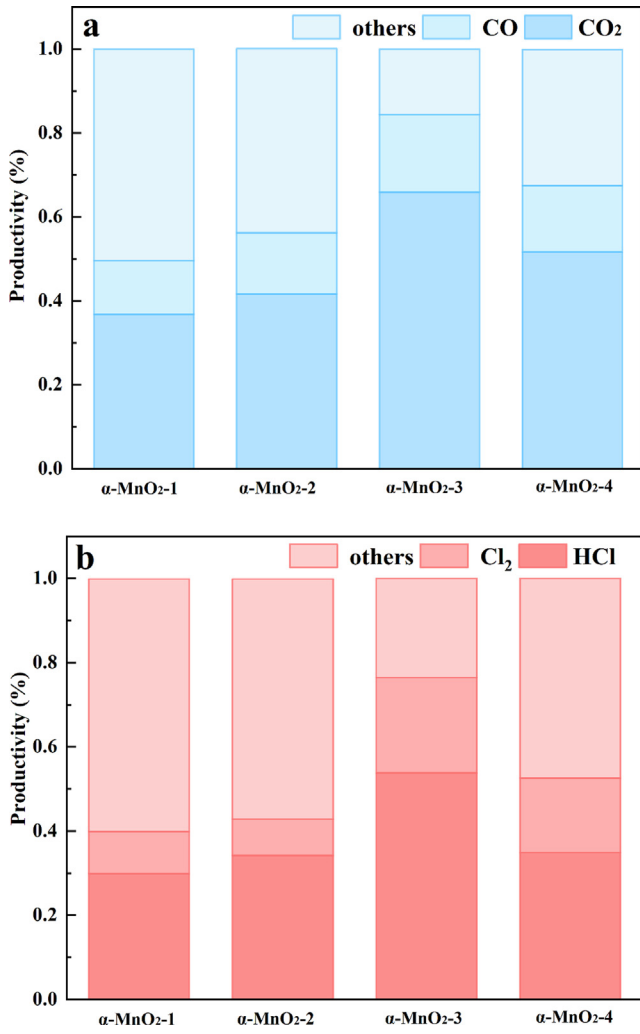


Fig. 2 The (a) carbon balance and (b) chlorine balance of different α-MnO₂ samples at 350 °C.

outlet were continuously measured by an infrared gas analyzer (Xi'an Juneng Corporation, China). NO_x conversion was evaluated by Eq. (1):

$$\text{NO}_x \text{ conversion (\%)} = \frac{[\text{NO}_x]_{\text{in}} - [\text{NO}_x]_{\text{out}}}{[\text{NO}_x]_{\text{in}}} \times 100\% \quad (1)$$

where [NO_x]_{in} and [NO_x]_{out} are the inlet and outlet concentration of NO_x, respectively.

2.2.2. Catalytic oxidation of DCE

The catalytic activity of DCE combustion was measured using a stainless-steel tubular (i.d.10 nm). 500 mg catalyst was selected for activity test. The reaction was conducted from 100 to 450 °C at a flow rate of 400 mL/min of feeding gases with 500 ppm DCE and 21 vol% O₂, corresponding to a gas hourly space velocity (GHSV) of 48 000 mL·g⁻¹·h⁻¹. DCE and products (CO and CO₂) were measured by an on-line gas chromatograph (GC9890) with ECD and FID. An on-line Cl₂ and HCl detectors (PN-2000, China) was used to analyse the concentrations of Cl₂ and HCl. DCE conversion, CO_x (CO₂ and CO) yield, HCl yield and Cl₂ yield were evaluated by the following Eqs. (2) to (6), respectively.

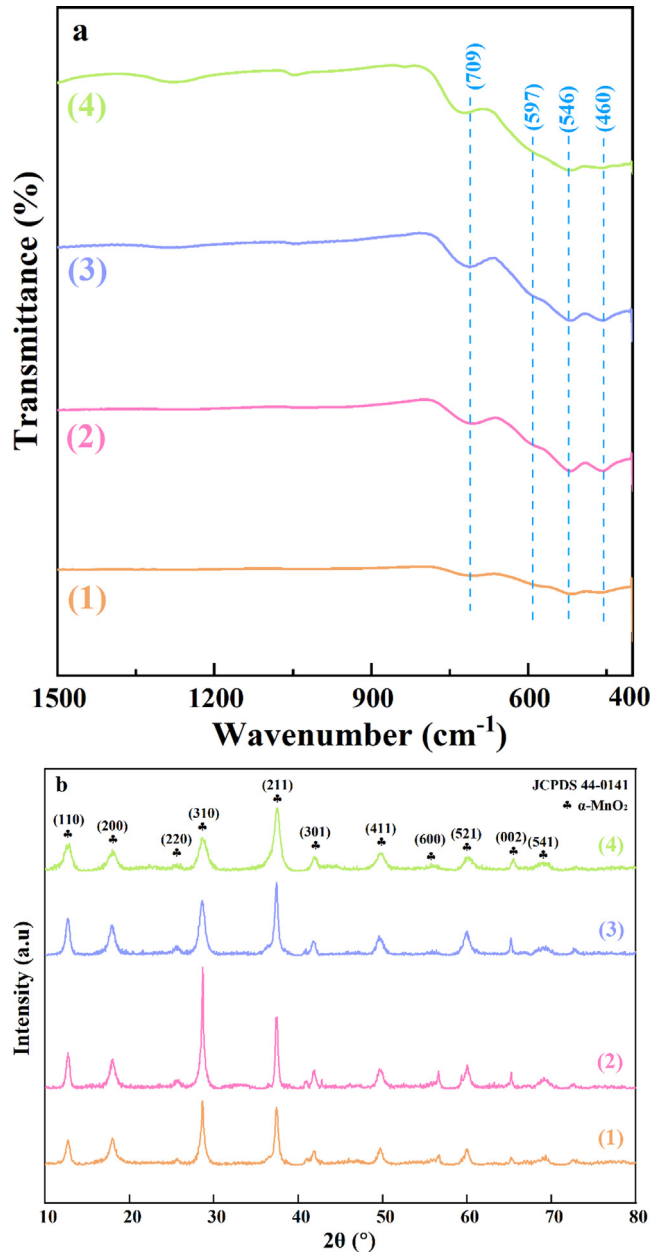


Fig. 3 (a) FT-IR spectra and (b) XRD patterns of (1) α-MnO₂-1, (2) α-MnO₂-2, (3) α-MnO₂-3 and (4) α-MnO₂-4.

$$\text{NO}_x \text{ conversion (\%)} = \frac{[\text{NO}_x]_{\text{in}} - [\text{NO}_x]_{\text{out}}}{[\text{NO}_x]_{\text{in}}} \times 100\% \quad (2)$$

$$\text{CO}_2 \text{ yield (\%)} = \frac{[\text{CO}_2]_{\text{out}}}{2[\text{DCE}]_{\text{in}}} \times 100\% \quad (3)$$

$$\text{CO yield (\%)} = \frac{\text{CO}_{\text{out}}}{2[\text{DCE}]_{\text{in}}} \times 100\% \quad (4)$$

$$\text{HCl yield (\%)} = \frac{\text{HCl}_{\text{out}}}{2[\text{DCE}]_{\text{in}}} \times 100\% \quad (5)$$

$$\text{Cl}_2 \text{ yield (\%)} = \frac{[\text{Cl}_2]_{\text{out}}}{[\text{DCE}]_{\text{in}}} \times 100\% \quad (6)$$

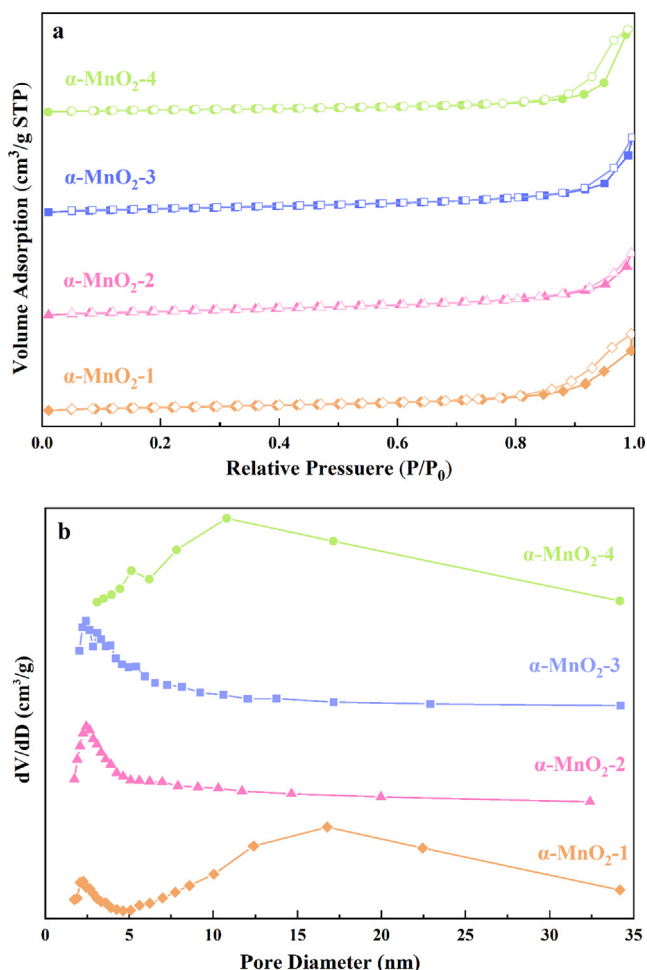


Fig. 4 N_2 adsorption/desorption curves (a) and BJH isotherms (b) of a series of α - MnO_2 samples.

where $[DCE]_{in}$ is the DCE inlet concentration of DCE. $[DCE]_{out}$, $[CO]_{out}$, $[CO_2]_{out}$, $[HCl]_{out}$ and $[Cl_2]_{out}$ are the outlet concentration of DCE, CO, CO_2 , HCl and Cl_2 , respectively.

2.3. Catalyst characterization

Fourier infrared spectrum (FT-IR) spectra was recorded in the range $400 \sim 2000 \text{ cm}^{-1}$ with a resolution of 4 cm^{-1} on a thermo scientific nicolet iS20 using the KBr pellet technique.

X-ray powder diffraction patterns (XRD) were obtained by Panalytical X'Pert'3 Powder diffractometer, equipped with Cu

$K\alpha$ X-ray radiation ($\lambda = 0.15406 \text{ nm}$). All the catalysts were scanned at 2θ range between 10° to 80° (rate of $2^\circ/\text{min}$).

The surface areas of the synthesized materials were determined by the Brunauer – Emmett – Teller (BET) method using ASAP 2460 3.01 instrument. Nitrogen physisorption experiments were carried out at 77 K after initial pretreatment of the samples by degassing at 300°C for 2 h.

Scanning electron microscopy (SEM) images have been studied using Schottky (ZEISS Gemini 300) equipment with a resolution of 10 kV and 50 kV.

Transmission electron microscopy (TEM) images were obtained from JEM-F200 electron field emission transmission electron microscope (JEOL, Japan) under 200 kV acceleration voltage.

X-ray photoelectron spectra (XPS) were carried out on thermo scientific system with Al $K\alpha$ radiation. The binding energy scale was corrected for surface charging by use of the C 1 s peak of contaminant carbon as reference at 284.8 eV.

Hydrogen temperature programmed reduction (H_2 -TPR) experiment was conducted on an AutoChem1 II 2920 instrument equipped with a thermal conductivity detector (TCD) to measure the consumption of H_2 . Before detection by the TCD, a 50 mg sample was pretreated under N_2 stream ($40 \text{ mL}\cdot\text{min}^{-1}$) at 300°C for 1 h, and then cooled to 50°C . A mixed stream with a 10 vol% H_2/Ar mixture ($50 \text{ mL}\cdot\text{min}^{-1}$) was introduced into the sample, and the sample was heated from room temperature to 800°C .

The NH_3 temperature-programmed desorption (NH_3 -TPD) was performed on an AutoChem1 II 2920 instrument. The catalyst was (100 mg) was pretreated in a N_2 ($50 \text{ mL}\cdot\text{min}^{-1}$) of at 300°C for 1 h, and then cooled to 50°C . Sample was treated with 10 % NH_3 diluted in N_2 ($30\text{--}50 \text{ mL}\cdot\text{min}^{-1}$) for 1 h to achieve adsorption saturation. The gas was switched back to He ($30 \text{ mL}\cdot\text{min}^{-1}$) for 1 h to purge the physically adsorbed species. Finally, the catalyst was heated from 50°C to 800°C at a rate of $10^\circ\text{C}\cdot\text{min}^{-1}$ in high purified N_2 ($30 \text{ mL}\cdot\text{min}^{-1}$).

3. Results and discussion

3.1. Catalytic performance

Fig. 1 showed the different catalytic performance of α - MnO_2 samples for NO_x reduction and DCE oxidation at the range of $100 \sim 450^\circ\text{C}$. For NO_x reduction, activity performance decreased as follows: α - MnO_2 -3 (63.5 %) > α - MnO_2 -4 (53.8 %) > α - MnO_2 -1 (45.2 %) \approx α - MnO_2 -2 (42.1 %) at 250°C . For DCE oxidation, T_{50} was chosen to compare the activity of these samples. T_{50} of DCE oxidation follows the order of

Table 1 Textural and surface property of catalysts.

Catalyst	S_{BET} (m^2/g)	V_{total} (cm^3/g)	D_p (nm)	$(Mn^{2+} + Mn^{3+})/Mn_T$	O_{ads}/O_{latt}	Acid amount (mmol/g)		Acid _T (mmol/g)
						I	II	
α - MnO_2 -1	72.6	0.2	10.1	0.5	0.4	0.8	0.6	1.4
α - MnO_2 -2	34.6	0.1	10.0	0.5	0.4	0.5	0.4	0.9
α - MnO_2 -3	44.1	0.1	12.6	0.7	0.6	1.1	1.2	2.3
α - MnO_2 -4	104.6	0.6	30.1	0.6	0.5	0.8	0.8	1.6

α-MnO₂-3 (276.4 °C) < α-MnO₂-4 (310.9 °C) < α-MnO₂-2 (337.3 °C) ≈ α-MnO₂-1 (348.6 °C). Thus, α-MnO₂-3 exhibited the highest catalytic activity for both NO_x reduction and DCE oxidation.

As exhibited in Fig. 2, in yield of CO₂ and CO, for α-MnO₂-3, it is remarkable to reveal 84.4 % of C₃H₈ was decomposed into CO_x. While for α-MnO₂-1, α-MnO₂-2 and α-MnO₂-4, C element in C₃H₈ was about 36.8 %, 41.6 % and 51.6 % converted to CO₂, and about 12.8 %, 14.6 % and 15.9 % converted to CO, respectively. In yield of HCl and Cl₂, for α-

MnO₂-3, 53.8 % of HCl and 22.7 % of Cl₂ were observed. That is, 76.5 % of DCE was total oxidized into inorganic chlorine products using α-MnO₂-3. However, for α-MnO₂-1, α-MnO₂-2 and α-MnO₂-4, Cl element in DCE were about 10.0 %, 8.6 % and 17.7 % converted to Cl₂, and about 29.9 %, 34.2 % and 34.9 % converted to HCl, respectively. There are about 60.0 %, 57.1 % and 47.4 % of chlorine remained as organic chlorine. Above all, α-MnO₂-3 displayed the best products selectivity.

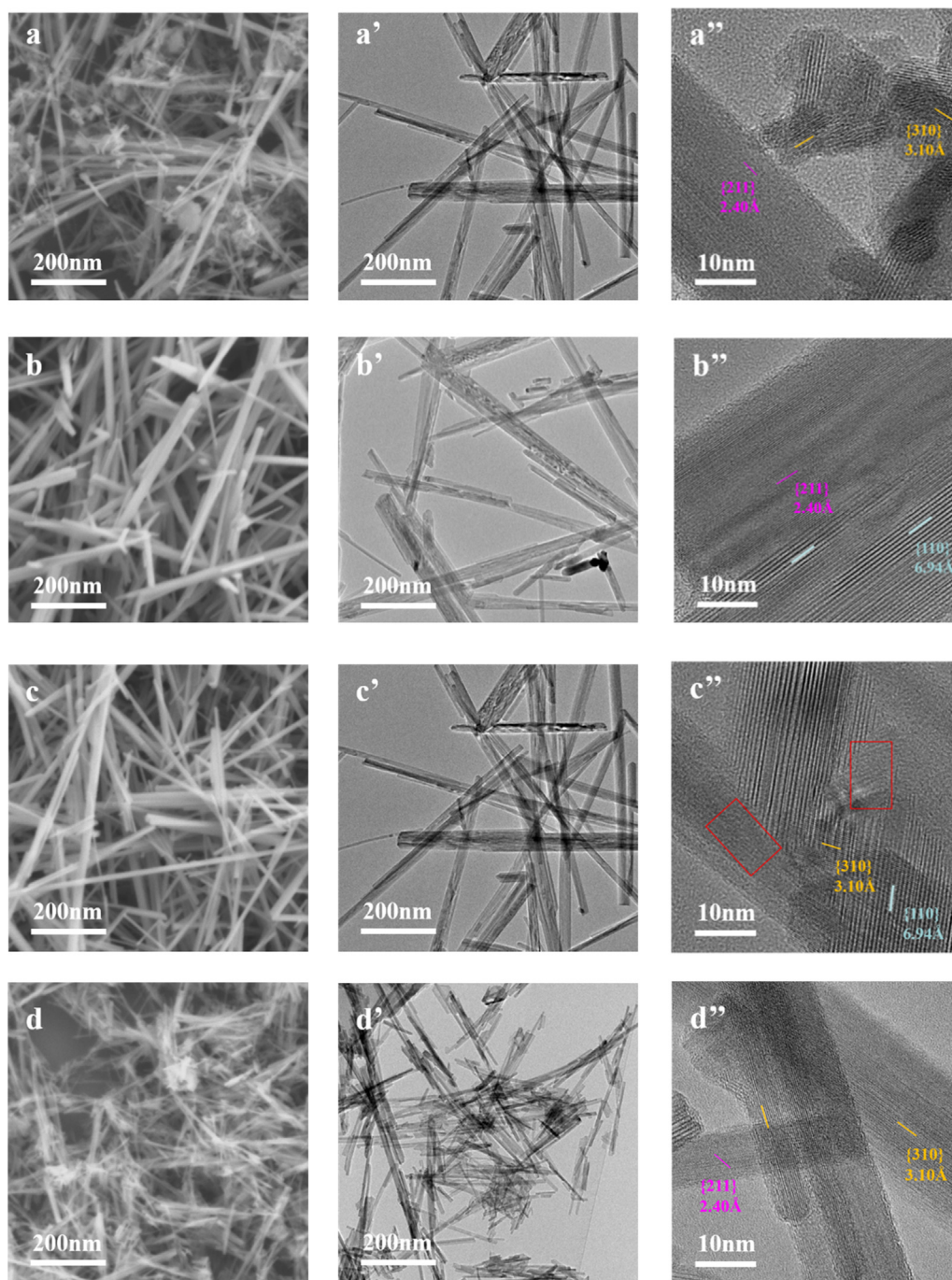


Fig. 5 SEM and TEM images of a series of α-MnO₂ samples under different magnifications. (a, a') α-MnO₂-1; (b, b') α-MnO₂-2; (c, c') α-MnO₂-3; (d, d') α-MnO₂-4.

3.2. Properties-reactivity relationship

3.2.1. Physical properties

FT-IR spectra of the synthesized materials are shown in Fig. 3a. The peaks in low wavenumbers between 800 cm^{-1} and 400 cm^{-1} are assigned to Mn-O lattice vibration (Yuan et al., 2009; Wang et al., 2019). Our samples showed the well-defined absorption peaks of MnO_2 at 469 cm^{-1} , 526 cm^{-1} , and 720 cm^{-1} as well as the weak defined shoulder at 597 cm^{-1} (King'ondeu et al., 2011; Chen et al., 2015; Liu et al., 2019b). Fig. 3b shows the XRD patterns of the as-prepared manganese oxide samples. Comparing to the XRD

patterns of the standard $\alpha\text{-MnO}_2$ (JCPDS 44-0141) (Cheng et al., 2017; Gao et al., 2017), it can deduce that all of the four samples could be well corresponding to the tetragonal $\alpha\text{-MnO}_2$ phase. The diffraction peaks at $2\theta = 12.9^\circ, 18.2^\circ, 25.8^\circ, 28.9^\circ, 37.6^\circ, 42.0^\circ, 49.9^\circ, 56.4^\circ, 60.3^\circ, 65.1^\circ,$ and 69.7° could be attributed to the (110), (200), (220), (310), (211), (301), (411), (600), (521), (002) and (541) plane, respectively. $\alpha\text{-MnO}_2$ presented three main peaks at $12.9^\circ, 28.9^\circ$ and 37.6° , which were assigned to the (110), (310) and (211) planes of $\alpha\text{-MnO}_2$ (JCPDS 44-0141). The peak intensity of (110) plane order decreased as follows: $\alpha\text{-MnO}_2\text{-3} > \alpha\text{-MnO}_2\text{-2} > \alpha\text{-MnO}_2\text{-4} > \alpha\text{-MnO}_2\text{-1}$. The intensity order of (310) plane is

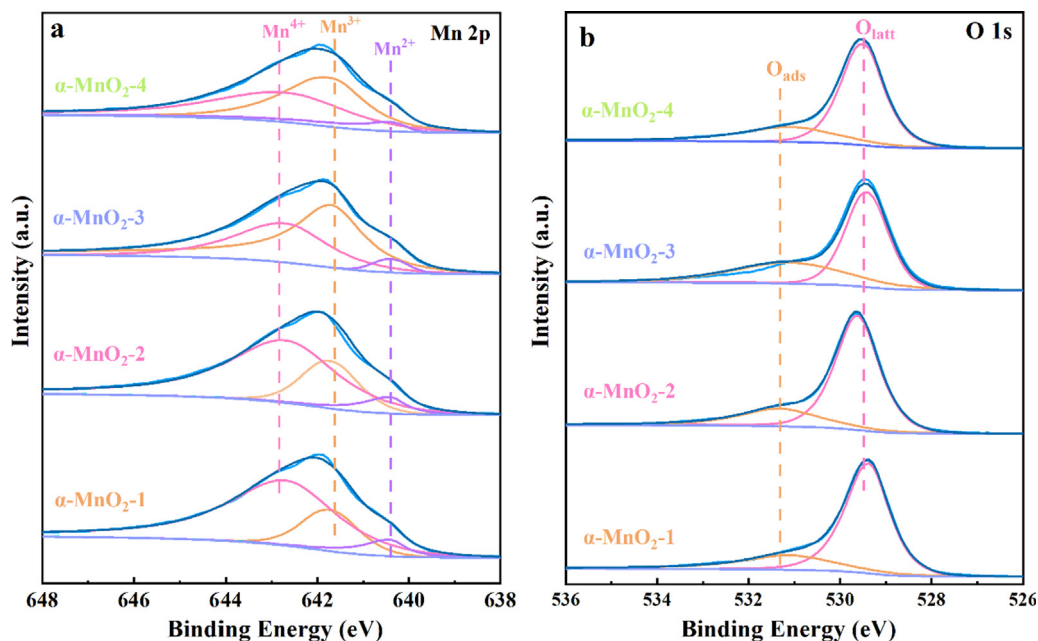


Fig. 6 XPS spectra of (a) Mn 2p and (b) O 1s regions for a series of $\alpha\text{-MnO}_2$ samples.

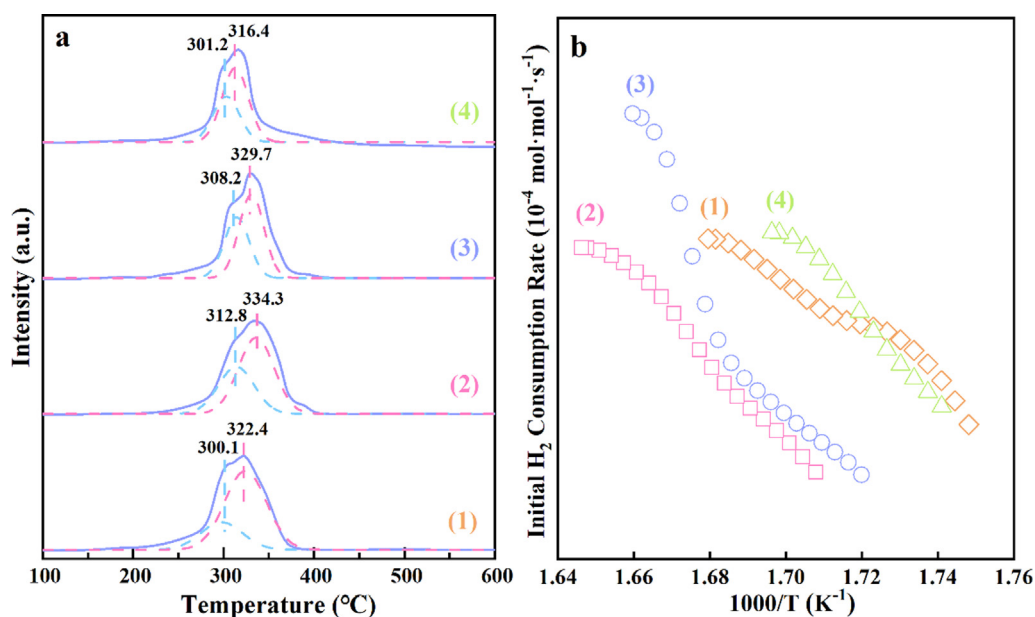


Fig. 7 (a) H_2 -TPR profiles and (b) initial H_2 consumption rates of (1) $\alpha\text{-MnO}_2\text{-1}$, (2) $\alpha\text{-MnO}_2\text{-2}$, (3) $\alpha\text{-MnO}_2\text{-3}$ and (4) $\alpha\text{-MnO}_2\text{-4}$.

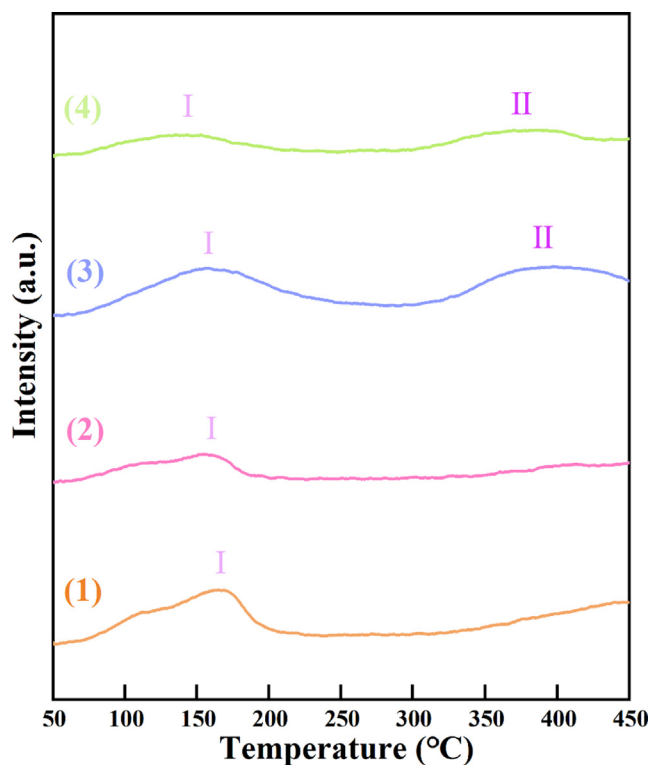


Fig. 8 NH₃-TPD profiles of (1) α-MnO₂-1, (2) α-MnO₂-2, (3) α-MnO₂-3 and (4) α-MnO₂-4.

as follows: α-MnO₂-2 > α-MnO₂-3 > α-MnO₂-1 > α-MnO₂-4. Interestingly, the peak intensity of (211) plane follows the order as α-MnO₂-3 > α-MnO₂-4 > α-MnO₂-2 > α-MnO₂-1, which is similar with the activity order of four samples. It indicates that (110) plane, (310) plane and (211) plane may be exposed active planes, in agreement with the findings of TEM. Besides, no diffraction peaks of other phases, such as β-MnO₂ and γ-MnO₂, are detected, implying that each catalyst is composed of α-MnO₂ phase. This result is consistent with the result of FT-IR.

The average pore size, pore volume and specific surface area of catalysts were measured by N₂ adsorption-desorption, and the results are presented in Fig. 4 and Table 1. N₂ adsorption-desorption isotherms of the samples type II characteristics with well-developed H₃ type hysteresis loops, confirming that the samples have mesoporous characteristics (Fig. 4a) (Sing, 1982). The samples possessed a mesopore distribution in the range of 2 ~ 35 nm in Fig. 4b. α-MnO₂-1 and α-MnO₂-4 presented a wide peak centered at from 5 nm to 35 nm, while α-MnO₂-2 and α-MnO₂-3 presented the peak centered at ca. 2.5 nm. In Table 1, the surface area order decreased as follows: α-MnO₂-4 (104.6 m²·g⁻¹) > α-MnO₂-1 (72.6 m²·g⁻¹) > α-MnO₂-3 (44.1 m²·g⁻¹) > α-MnO₂-2 (34.6 m²·g⁻¹). The pore volume of order was as follows: α-MnO₂-4 (0.6 cm³·g⁻¹) > α-MnO₂-1 (0.2 cm³·g⁻¹) > α-MnO₂-3 (0.1 cm³·g⁻¹) = α-MnO₂-2 (0.1 cm³·g⁻¹). The difference in preparation condition leads to a big difference in surface area of the α-MnO₂ samples.

To further analyze the morphologies and surface structures of the catalysts, the SEM and TEM images of four samples are shown in Fig. 5. It should be noted that the wire-like morphol-

ogy can be differentiated from the rod-like morphology in terms of the bending or straight shape (Wang et al., 2012). Fig. 5 (a) and (d) showed that both α-MnO₂-1 and α-MnO₂-4 are presented as stacking-nanowires, while Fig. 5 (b) and (c) exhibited nanorod-like appearance of α-MnO₂-2 and α-MnO₂-3 with uniform distribution. It should be noted that the surface area of wire-like morphology can be much larger than the rod-like morphology. The well-identified periodic lattice fringes of 2.40 Å, 3.10 Å and 6.94 Å are corresponding to the interplanar distance of (211), (310) and (110) facets of α-MnO₂, respectively. Whereas, severe blurring of the lattice fringes were also detected (highlighted by red rectangles) in α-MnO₂-3. It is worth noting that large amount of point defects on α-MnO₂ could obscure the distorted lattice fringes, which may result from the existence of oxygen vacancies on catalyst surfaces (Huang et al., 2018). The morphologies of samples are consistent with the findings of XRD.

3.2.2. Chemical properties

XPS measurements were carried out to identify the surface species of α-MnO₂ samples. Fig. 6a illustrated Mn 2p spectra of four samples. Peaks at 642.7, 641.7 and 640.4 eV can be attributed to Mn⁴⁺, Mn³⁺ and Mn²⁺, respectively (Si et al., 2015; Ma et al., 2017; Zhang et al., 2022). In Table 1, the proportion of low valence Mn (Mn³⁺ and Mn²⁺) followed the order (Table 1): α-MnO₂-3 (0.7) > α-MnO₂-4 (0.6) > α-MnO₂-2 (0.5) = α-MnO₂-1 (0.5). Low valence Mn content is an indicator of surface oxygen vacancies (Yang et al., 2020). Additionally, Mn²⁺-O and Mn³⁺-O bonds are weaker than Mn⁴⁺-O (Zhang, 1982). Large proportion of low valence Mn results in longer and weaker Mn-O bonds on the surface of α-MnO₂-3 (Yang et al., 2020). It suggests that oxygen atoms on its surface are more likely to be released to participate in oxidation. In addition, the existence of surface low valence Mn would promote dissociation and activation of circumambient oxygen atoms (Yang et al., 2020).

The XPS spectra of O 1s of the samples are shown in Fig. 6b. As reported previously, the peak around 529.0 ~ 530.0 eV is typical for O_{latt} in a coordinatively saturated environment, while the peak around 531.0 ~ 532.0 eV can be attributed to the O_{ads} in a low-coordinated environment (Tang et al., 2010; Wang et al., 2011; Yang et al., 2022a). As shown in Table 1, the O_{ads}/O_{latt} molar ratio for all α-MnO₂ catalysts follows the order of α-MnO₂-3 (0.6) > α-MnO₂-4 (0.5) > α-MnO₂-2 (0.4) = α-MnO₂-1 (0.4), which is consistent with the catalytic activity results. As we know that O_{ads} performs high activities and makes an important impact in SCR reaction because of its higher mobility than O_{latt} (Zhang et al., 2020). On the basis of the Mars-van Krevelen mechanism, the emergence and annihilation of oxygen vacancies is the key step of VOC oxidation. Adsorbed oxygen species participate in the redox cycle of the vacancies from gaseous-adsorbed oxygen transformation (Huang et al., 2015). Surface adsorbed oxygen are relevant to the formation of Mn³⁺ and Mn²⁺ and are more active than lattice oxygen at low temperatures (Wang et al., 2012). Thus, α-MnO₂-3 might be highly active in DCE oxidation owing to large numbers of low valence Mn cations and adsorbed oxygen species.

H₂-TPR measurement is carried out to analyze the reducibility of different α-MnO₂ samples and the results are presented in Fig. 7. As shown in Fig. 7a, Two reduction peaks

(I, II) could be due to the reduction of Mn^{4+} to Mn^{3+} and Mn^{3+} to Mn^{2+} , respectively (Yang et al., 2020). The initial H_2 consumption rate was calculated to better evaluate the reducibility of these samples, as depicted in Fig. 7b. It was clearly seen that the initial H_2 consumption rates of the samples decreased in the order of $\alpha\text{-MnO}_2\text{-3} > \alpha\text{-MnO}_2\text{-4} > \alpha\text{-MnO}_2\text{-1} > \alpha\text{-MnO}_2\text{-2}$. The lower reduction temperature and the larger initial H_2 consumption rate indicate a better low-

temperature redox ability (Chen et al., 2017; Gong et al., 2017).

NH_3 -TPD experiments are taken to analyze the acidities of the four types of $\alpha\text{-MnO}_2$ and the results are shown in Fig. 8 and Table 1. As shown in Fig. 8, NH_3 -TPD curves of $\alpha\text{-MnO}_2$ samples exhibited two desorption peaks (labeled as I and II). The desorption peak I at low temperature is attributed to the desorption of NH_3 from weak acid sites and the desorp-

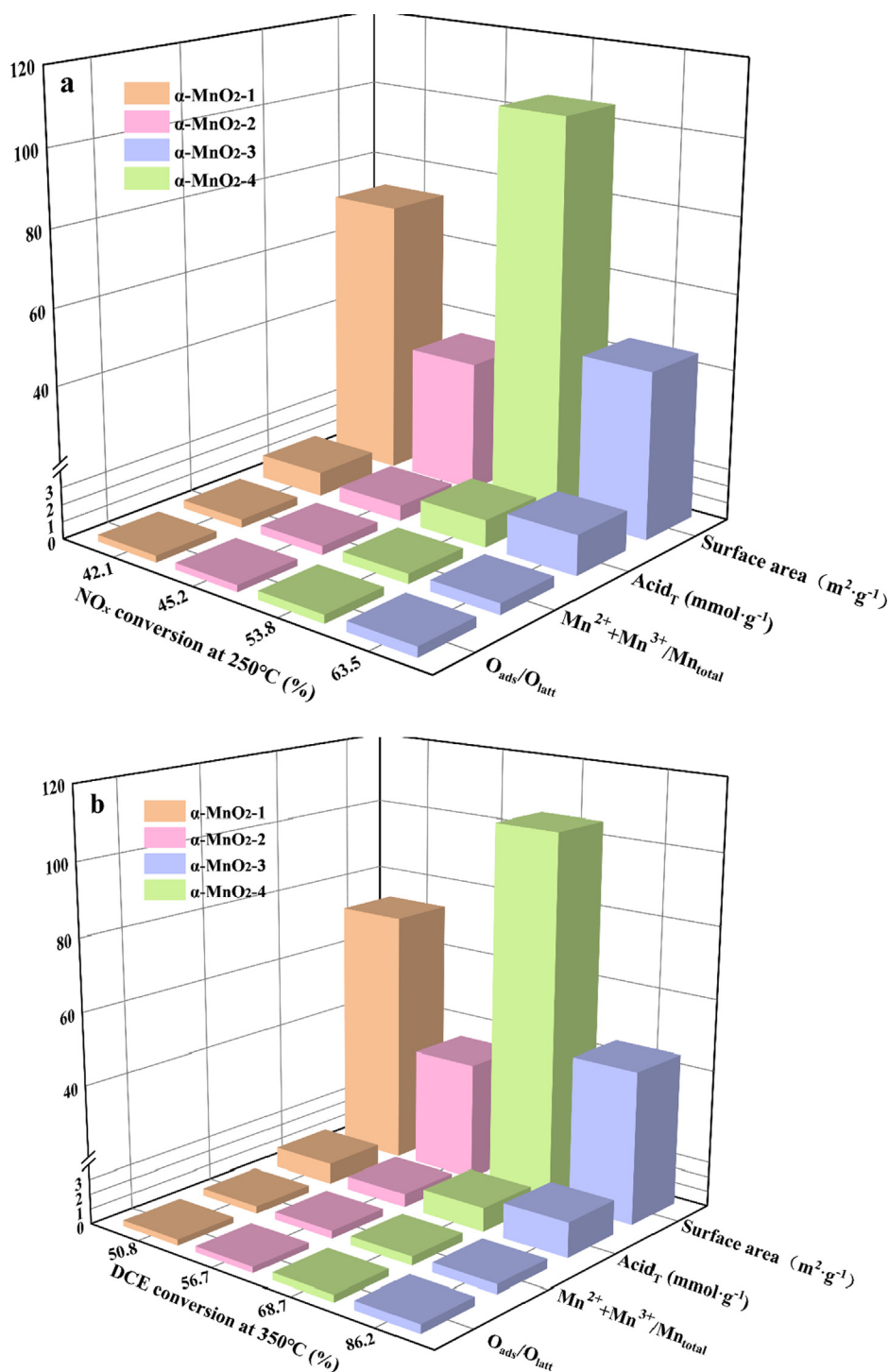


Fig. 9 The relationship between catalytic activities for NO_x reduction (a) and DCE oxidation (b).

tion of physisorbed NH₃, the desorption peak II at middle temperature is assigned to the desorption of NH₃ from middle strong acid sites (Fang et al., 2013; Yao et al., 2017). It is worth noting that two desorption peaks of α-MnO₂-3 and α-MnO₂-4 belong to weak acid site and middle strong acid site at below 450°C. The quantitative analysis data of NH₃-TPD was summarized in Table 1. It was reported that the quantity of the desorption peak was proportional to the strength of acid site (Zhang et al., 2020). Hence, as seen in Fig. 8, the quantity of peaks can be ranked by α-MnO₂-3 > α-MnO₂-4 > α-MnO₂-1 > α-MnO₂-2, implying the order of acid site numbers. α-MnO₂-3 catalyst not only shows two acid sites at 145°C and 350°C, but also presents the largest amount of acid sites among these catalysts, which is basically consistent with the activity test of NO_x reduction.

The possible properties-reactivity relationship of four α-MnO₂ samples was illustrated in Fig. 9. In this work, O_{ads}/O_{latt}, low valence Mn content and total acidity were positively related to activity of the samples. However, surface area, pore structure and redox properties are not the key factors in our study.

4. Conclusion

α-MnO₂-3 catalyst presented the best performance among a series of α-MnO₂ for both the catalytic reduction of NO_x reduction and DCE oxidation. The O_{ads}/O_{latt}, the proportion of low valence Mn content and total acidity are the crucial factors for the activity of α-MnO₂. The maximum conversion of NO_x achieved 63.5 % at 250°C and DCE achieved 80 % at 338°C on α-MnO₂-3 catalyst, respectively. As for the yield of carbon and chlorine, α-MnO₂-3 also exhibits highest yield, which implies that α-MnO₂-3 may be a potential catalyst for removal of NO_x and VOCs.

Declaration of interests

The authors declare that they have no know competing financial interests or personal relationships that could have appeared to influence the work reported in this paper.

Acknowledgments

This work was financially supported by Zhejiang Provincial Natural Science Foundation of China (LGF22B070005) and Innovation and Entrepreneurship Talent Project of Jiangsu Province (JSSCRC2021236).

References

Alzakay, M.A.M., Li, D.X., 2021. Production of the complete fertilizer with simultaneously removing sulfur oxides and nitrogen oxides using yellow phosphorus. *Arab. J. Chem.* 14, 4. <https://doi.org/10.1016/j.arabjc.2021.103043>.

Chen, J., Chen, X., Xu, W., Xu, Z., Chen, J., Jia, H., Chen, J., 2017. Hydrolysis driving redox reaction to synthesize Mn-Fe binary oxides as highly active catalysts for the removal of toluene. *Chem. Eng. J.* 330, 281–293. <https://doi.org/10.1016/j.cej.2017.07.147>.

Chen, C.H., Njagi, E.C., Chen, S.Y., Horvath, D.T., Xu, L., Morey, A., Mackin, C., Joesten, R., Suib, S.L., 2015. Structural distortion of molybdenum-doped manganese oxide octahedral molecular sieves for enhanced catalytic performance. *Inorg. Chem.* 54, 10163–10171. <https://doi.org/10.1021/acs.inorgchem.5b00906>.

Chen, J., Yang, Y., Zhao, S., Bi, F., Song, L., Liu, N., Xu, J., Wang, Y., Zhang, X., 2022. Stable Black Phosphorus Encapsulation in Porous Mesh-like UiO-66 Promoted Charge Transfer for Photocatalytic Oxidation of Toluene and o-Dichlorobenzene: Performance, Degradation Pathway, and Mechanism. *ACS Catalysis* 12, 8069–8081. <https://doi.org/10.1021/acscatal.2c01375>.

Cheng, G., Yu, L., He, B., Sun, M., Zhang, B., Ye, W., Lan, B., 2017. Catalytic combustion of dimethyl ether over alpha-MnO₂ nanostructures with different morphologies. *Appl. Surf. Sci.* 409, 223–231. <https://doi.org/10.1016/j.apsusc.2017.02.218>.

Fang, R., Huang, W., Huang, H., Feng, Q., He, M., Ji, J., Liu, B., Leung, D.Y.C., 2019. Efficient MnO_x/SiO₂@AC catalyst for ozone-catalytic oxidation of gaseous benzene at ambient temperature. *Appl. Surf. Sci.* 470, 439–447. <https://doi.org/10.1016/j.apsusc.2018.11.146>.

Fang, C., Zhang, D., Cai, S., Zhang, L., Huang, L., Li, H., Maitarad, P., Shi, L., Gao, R., Zhang, J., 2013. Low-temperature selective catalytic reduction of NO with NH₃ over nanoflaky MnO_x on carbon nanotubes in situ prepared via a chemical bath deposition route. *Nanoscale* 5, 9199–9207. <https://doi.org/10.1039/C3NR02631K>.

Gao, F.Y., Tang, X.L., Yi, H.H., Chu, C., Li, N., Li, J.Y., Zhao, S.Z., 2017. In-situ DRIFTS for the mechanistic studies of NO oxidation over alpha-MnO₂, beta-MnO₂ and gamma-MnO₂ catalysts. *Chem. Eng. J.* 322, 525–537. <https://doi.org/10.1016/j.cej.2017.04.006>.

Gong, P., Xie, J., Fang, D., Han, D., He, F., Li, F., Qi, K., 2017. Effects of surface physicochemical properties on NH₃-SCR activity of MnO₂ catalysts with different crystal structures. *Chin. J. Catal.* 38, 1925–1934. [https://doi.org/10.1016/s1872-2067\(17\)62922-x](https://doi.org/10.1016/s1872-2067(17)62922-x).

He, C., Cheng, J., Zhang, X., Douthwaite, M., Pattison, S., Hao, Z., 2019. Recent advances in the catalytic oxidation of volatile organic compounds: a review based on pollutant sorts and sources. *Chem. Rev.* 119, 4471–4568. <https://doi.org/10.1021/acs.chemrev.8b00408>.

Huang, N., Qu, Z., Dong, C., Qin, Y., Duan, X., 2018. Superior performance of α@β-MnO₂ for the toluene oxidation: Active interface and oxygen vacancy. *Appl. Catal. A* 560, 195–205. <https://doi.org/10.1016/j.apcata.2018.05.001>.

Huang, H.B., Xu, Y., Feng, Q.Y., Leung, D.Y.C., 2015. Low temperature catalytic oxidation of volatile organic compounds: a review. *Catal. Sci. Technol.* 5, 2649–2669. <https://doi.org/10.1039/c4cy01733a>.

Khan, A.M., Wick, L.Y., Thullner, M., 2018. Applying the Rayleigh Approach for Stable Isotope-Based Analysis of VOC Biodegradation in Diffusion-Dominated Systems. *Environ. Sci. Technol.* 52, 7785–7795. <https://doi.org/10.1021/acs.est.8b01757>.

Kim, S.C., Shim, W.G., 2010. Catalytic combustion of VOCs over a series of manganese oxide catalysts. *Appl. Catal. B* 98, 180–185. <https://doi.org/10.1016/j.apcatb.2010.05.027>.

King'onde, C.K., Opmembe, N., Chen, C.H., Ngala, K., Huang, H., Iyer, A., Garces, H.F., Suib, S.L., 2011. Manganese oxide octahedral molecular sieves (OMS-2) multiple framework substitutions: a new route to OMS-2 particle size and morphology control. *Adv. Funct. Mater.* 21, 312–323. <https://doi.org/10.1002/adfm.201001020>.

Kulkarni, P.S., Crespo, J.G., Afonso, C.A., 2008. Dioxins sources and current remediation technologies—a review. *Environ. Int.* 34, 139–153. <https://doi.org/10.1016/j.envint.2007.07.009>.

Li, J., Lv, Z., Du, L., Li, X., Hu, X., Wang, C., Niu, Z., Zhang, Y., 2017. Emission characteristic of polychlorinated dibenzo-p-dioxins and polychlorinated dibenzofurans (PCDD/Fs) from medical waste incinerators (MWIs) in China in 2016: A comparison between higher emission levels of MWIs and lower emission levels of MWIs. *Environ. Pollut.* 221, 437–444. <https://doi.org/10.1016/j.envpol.2016.12.009>.

Liu, X., Chen, L., Zhu, T., Ning, R., 2019c. Catalytic oxidation of chlorobenzene over noble metals (Pd, Pt, Ru, Rh) and the distributions of polychlorinated by-products. *J. Hazard. Mater.* 363, 90–98. <https://doi.org/10.1016/j.jhazmat.2018.09.074>.

- Liu, G., Han, D., Cheng, J., Feng, Y., Quan, W., Yang, L., Saito, K., 2019a. Performance of C₂H₄ reductant in activated-carbon-supported MnO_x-based SCR catalyst at low temperatures. *Energies* 12, 123. <https://doi.org/10.3390/en12010123>.
- Liu, G., Wang, H., Feng, N., Chen, L., Yu, J., Meng, J., Fang, F., Wang, L., Wan, H., Guan, G., 2019b. Construction of substrate-dependent 3D structured MnO₂ catalysts for diesel soot elimination. *Appl. Surf. Sci.* 484, 197–208. <https://doi.org/10.1016/j.apsusc.2019.04.090>.
- Ma, C., Wen, Y., Rong, C., Zhang, N., Zheng, J., Chen, B.H., 2017. δ-MnO₂ with an ultrahigh Mn⁴⁺ fraction is highly active and stable for catalytic wet air oxidation of phenol under mild conditions. *Catal. Sci. Technol.* 7, 3200–3204. <https://doi.org/10.1039/C7CY00774D>.
- More, P.M., Dongare, M.K., Umbarkar, S.B., Granger, P., Dujardin, C., 2018. Bimetallic Au-Ag/Al₂O₃ as efficient catalysts for the hydrocarbon selective reduction of NO_x from lean burn engine exhaust. *Catal. Today* 306, 23–31. <https://doi.org/10.1016/j.cattod.2016.12.002>.
- Ni, Y., Zhang, H., Fan, S., Zhang, X., Zhang, Q., Chen, J., 2009. Emissions of PCDD/Fs from municipal solid waste incinerators in China. *Chemosphere* 75, 1153–1158. <https://doi.org/10.1016/j.chemosphere.2009.02.051>.
- Pan, H., Jian, Y., Chen, C., He, C., Hao, Z., Shen, Z., Liu, H., 2017. Sphere-shaped Mn₃O₄ catalyst with remarkable low-temperature activity for Methyl-Ethyl-Ketone combustion. *Environ. Sci. Technol.* 51, 6288–6297. <https://doi.org/10.1021/acs.est.7b00136>.
- Piumetti, M., Fino, D., Russo, N., 2015. Mesoporous manganese oxides prepared by solution combustion synthesis as catalysts for the total oxidation of VOCs. *Appl. Catal. B* 163, 277–287. <https://doi.org/10.1016/j.apcatb.2014.08.012>.
- Santos, V.P., Pereira, M.F.R., Órfão, J.J.M., Figueiredo, J.L., 2010. The role of lattice oxygen on the activity of manganese oxides towards the oxidation of volatile organic compounds. *Appl. Catal. B* 99, 353–363. <https://doi.org/10.1016/j.apcatb.2010.07.007>.
- Shao, J., Wang, Z., Liu, P., Lin, F., Zhu, Y., He, Y., Cen, K., 2021. Interplay effect on simultaneous catalytic oxidation of NO and toluene over different crystal types of MnO₂ catalysts. *P COMBUST INST* 38, 5433–5441. <https://doi.org/10.1016/j.proci.2020.06.040>.
- Si, W., Wang, Y., Peng, Y., Li, J., 2015. Selective dissolution of a-site cations in ABO(3) perovskites: a new path to high-performance catalysts. *Angew. Chem. Int. Ed. Engl.* 54, 7954–7957. <https://doi.org/10.1002/anie.201502632>.
- Sing, K.S.W., 1982. Reporting physisorption data for gas/solid systems with special reference to the determination of surface area and porosity (Provisional). *Pure Appl. Chem.* 54, 2201–2218. <https://doi.org/10.1351/pac198254112201>.
- Tang, X., Li, J., Hao, J., 2010. Significant enhancement of catalytic activities of manganese oxide octahedral molecular sieve by marginal amount of doping vanadium. *Catal. Commun.* 11, 871875. <https://doi.org/10.1016/j.catcom.2010.03.011>.
- Wang, F., Dai, H., Deng, J., Bai, G., Ji, K., Liu, Y., 2012. Manganese oxides with rod-, wire-, tube-, and flower-like morphologies: highly effective catalysts for the removal of toluene. *Environ. Sci. Technol.* 46, 4034–4041. <https://doi.org/10.1021/es204038j>.
- Wang, Y., Shen, S.G., Li, M.N., Sun, Y.J., Li, B.B., Ma, X.P., Zhou, Z.J., Guo, C.Y., 2019. Urea hydrolysis over α-MnO₂ catalyst: preparation, characterizations and influencing factors. *Catal. Lett.* 149, 2032–2042. <https://doi.org/10.1007/s10562-019-02730-w>.
- Wang, C., Sun, L., Cao, Q., Hu, B., Huang, Z., Tang, X., 2011. Surface structure sensitivity of manganese oxides for low-temperature selective catalytic reduction of NO with NH₃. *Appl. Catal. B* 101, 598–605. <https://doi.org/10.1016/j.apcatb.2010.10.034>.
- Wu, S., Zhou, J., Pan, Y., Zhang, J., Zhang, L., Ohtsuka, N., Motegi, M., Yonemochi, S., Oh, K., Hosono, S., Qian, G., 2016. Dioxin distribution characteristics and health risk assessment in different size particles of fly ash from MSWIs in China. *Waste Manage.* (Oxford) 50, 113–120. <https://doi.org/10.1016/j.wasman.2016.01.038>.
- Xu, J.Q., Qin, Y.H., Wang, H.L., Guo, F., Xie, J.Q., 2020. Recent advances in copper-based zeolite catalysts with low-temperature activity for the selective catalytic reduction of NO_x with hydrocarbons. *New J. Chem.* 44, 817–831. <https://doi.org/10.1039/c9nj04735b>.
- Yang, W.H., Su, Z.A., Xu, Z.H., Yang, W.N., Peng, Y., Li, J.H., 2020. Comparative study of alpha-, beta-, gamma- and delta-MnO₂ on toluene oxidation: Oxygen vacancies and reaction intermediates. *Appl. Catal., B* 260. <https://doi.org/10.1016/j.apcatb.2019.118150>.
- Yang, Y., Zhao, S., Bi, F., Chen, J., Wang, Y., Cui, L., Xu, J., Zhang, X., 2022a. Highly efficient photothermal catalysis of toluene over Co₃O₄/TiO₂ p-n heterojunction: The crucial roles of interface defects and band structure. *Appl. Catal. B* 315. <https://doi.org/10.1016/j.apcatb.2022.121550>.
- Yang, Y., Zhao, S., Cui, L., Bi, F., Zhang, Y., Liu, N., Wang, Y., Liu, F., He, C., Zhang, X., 2022b. Recent advancement and future challenges of photothermal catalysis for VOCs elimination: From catalyst design to applications. *Green Energy & Environ.* <https://doi.org/10.1016/j.gee.2022.02.006>.
- Yao, X., Kong, T., Yu, S., Li, L., Yang, F., Dong, L., 2017. Influence of different supports on the physicochemical properties and denitration performance of the supported Mn-based catalysts for NH₃-SCR at low temperature. *Appl. Surf. Sci.* 402, 208–217. <https://doi.org/10.1016/j.apsusc.2017.01.081>.
- Ye, Z., Giraudon, J.-M., Nuns, N., Abdallah, G., Addad, A., Morent, R., De Geyter, N., Lamonier, J.-F., 2021. Preferential dissolution of copper from Cu-Mn oxides in strong acid medium: Effect of the starting binary oxide to get new efficient copper doped MnO₂ catalysts in toluene oxidation. *Appl. Surf. Sci.* 537. <https://doi.org/10.1016/j.apsusc.2020.147993>.
- Ye, Z., Wang, G., Giraudon, J.-M., Nikiforov, A., Chen, J., Zhao, L., Zhang, X., Wang, J., 2022. Investigation of Cu-Mn catalytic ozonation of toluene: Crystal phase, intermediates and mechanism. *J. Hazard. Mater.* 424. <https://doi.org/10.1016/j.jhazmat.2021.127321>.
- Yu, F., Wang, C.H., Li, Y.Y., Ma, H., Wang, R., Liu, Y.C., Suzuki, N., Terashima, C., Ohtani, B., Ochiai, T., Fujishima, A., Zhang, X. T., 2020. Enhanced Solar Photothermal Catalysis over Solution Plasma Activated TiO₂. *Adv. Sci.* 7. <https://doi.org/10.1002/adv.202000204>.
- Yuan, J., Liu, Z.-H., Qiao, S., Ma, X., Xu, N., 2009. Fabrication of MnO₂-pillared layered manganese oxide through an exfoliation/reassembling and oxidation process. *J. Power Sources* 189, 1278–1283. <https://doi.org/10.1016/j.jpowsour.2008.12.148>.
- Zhang, Y., 1982. Electronegativities of elements in valence states and their applications. *Inorg. Chem.* 21, 3886–3889. <https://doi.org/10.1021/ic00141a005>.
- Zhang, B., Chen, D., Liu, H., Zou, X., Chen, T., 2020. Selective catalytic reduction of NO with NH₃ over high purity palygorskite-supported MnO₂ with different crystal structures. *Aerosol Air Qual. Res.* 20, 1155–1165. <https://doi.org/10.4209/aaqr.2020.03.0099>.
- Zhang, X., Xiang, S., Du, Q., Bi, F., Xie, K., Wang, L., 2022. Effect of calcination temperature on the structure and performance of rod-like MnCeO_x derived from MOFs catalysts. *Mol. Catal.* 522. <https://doi.org/10.1016/j.mcat.2022.112226>.
- Zhao, Q., Zhao, Z., Rao, R., Yang, Y., Ling, S., Bi, F., Shi, X., Xu, J., Lu, G., Zhang, X., 2022. Universitetet i Oslo-67 (UiO-67)/graphite oxide composites with high capacities of toluene: Synthesis strategy and adsorption mechanism insight. *J. Colloid Interface Sci.* 627, 385–397. <https://doi.org/10.1016/j.jcis.2022.07.059>.
- Zhu, F., Li, X., Lu, J.-W., Hai, J., Zhang, J., Xie, B., Hong, C., 2018. Emission characteristics of PCDD/Fs in stack gas from municipal solid waste incineration plants in Northern China. *Chemosphere* 200, 23–29. <https://doi.org/10.1016/j.chemosphere.2018.02.092>.